

THE INTRINSIC ABSORBER IN QSO 2359–1241: KECK AND HST OBSERVATIONS

Nahum Arav¹, Michael S. Brotherton²³, Robert H. Becker^{1,3}, Michael D. Gregg^{1,3},
Richard L. White⁴, Trevor Price^{1,3}, Warren Hack⁴

ABSTRACT

We present detailed analyses of the absorption spectrum seen in QSO 2359–1241 (NVSS J235953–124148). Keck HIRES data reveal absorption from twenty transitions arising from: He I, Mg I, Mg II, Ca II, and Fe II. HST data show broad absorption lines (BALs) from Al III λ 1857, C IV λ 1549, Si IV λ 1397, and N V λ 1240. Absorption from excited Fe II states constrains the temperature of the absorber to $2000 \lesssim T \lesssim 10,000$ K and puts a lower limit of 10^5 cm $^{-3}$ on the electron number density. Saturation diagnostics show that the real column densities of He I and Fe II can be determined, allowing to derive meaningful constraints on the ionization equilibrium and abundances in the flow. The ionization parameter is constrained by the iron, helium and magnesium data to $-3.0 \lesssim \log(U) \lesssim -2.5$ and the observed column densities can be reproduced without assuming departure from solar abundances. From comparison of the He I and Fe II absorption features we infer that the outflow seen in QSO 2359–1241 is not shielded by a hydrogen ionization front and therefore that the existence of low-ionization species in the outflow (e.g., Mg II, Al III, Fe II) does not necessitate the existence of such a front. We find that the velocity width of the absorption systematically increases as a function of ionization and to a lesser extent with abundance. Complementary analyses of the radio and polarization properties of the object are discussed in a companion paper (Brotherton et al. 2000).

Subject headings: quasars: absorption lines

¹Physics Department, University of California, Davis, CA 95616 I: arav@astro.berkeley.edu

²Kitt Peak National Observatory, 950 North Cherry Avenue, P. O. Box 26732, Tuscon, AZ 85726

³IGPP LLNL, L-413, P.O. Box 808, Livermore, CA 94550

⁴Space Telescope Science Institute, Baltimore, MD 21218

1. INTRODUCTION

The radio source NVSS J235953-124148 (z=0.868), hereafter QSO 2359–1241, is unique among quasars. It shows intrinsic absorption from: Mg II and Fe II, which appear in less than 1% of optically selected quasars; Mg I, which is even less frequent; and from a meta-stable He I level, which is only seen in two or three other AGNs. We use the term “intrinsic absorption” following the definition given by Hamann et al (1997) and Barlow (1997). Whenever this absorption is significantly blue-shifted with respect to the systemic redshift of the quasar, we interpret it as rising from an outflow connected with the AGN. In § 2 we establish the intrinsic nature of the absorption seen in QSO 2359–1241. Besides its rare absorption features, QSO 2359–1241 has very high intrinsic polarization ($\sim 5\%$) and is moderately reddened (Brotherton et al. 2000). A low-resolution Keck spectrum of the object is shown in figure 1.

By exhibiting absorption from Mg II and Al III QSO 2359–1241 is classified as a low-ionization BALQSO. Low-ionization BALQSOs were studied by Boroson and Meyers (1992), Voit, Weymann and Korista (1993) Wampler, Chugai & Petitjean (1995); Becker et al. (1997) and de Kool et al. (2000), among others. All the low-ionization BALQSOs show absorption from Mg II, but only a subset of these show absorption from Fe II (Prominent examples include: QSO 0059–2735, Wampler et al. 1995; Arp 102B, Halpern et al 1996; FIRST 0840+3633 and 1556+3517, Becker et al. 1997; QSO 1044+3656, de Kool et al. 2000). An even smaller subset shows Mg I in absorption (Arp 102B, QSO 1044+3656). For example, from the six objects studied by Voit, Weymann and Korista (1993) only one (QSO 0059–2735) shows Fe II absorption and none show Mg I absorption. QSO 2359–1241 shows absorption features from all these ions as well as from He I. In the discussion we elaborate on the conditions needed for detecting these lines (both physical and observational) and argue that even though the low-ionization features in QSO 2359–1241 are too narrow to be classified as classical BALs, they are definitely part of a BAL outflow because of their association with the much wider high-ionization absorption troughs (C IV $\lambda 1549$ and Si IV $\lambda 1397$) seen in the ultraviolet spectrum.

The ions detected in absorption and their unique characteristics make QSO 2359–1241 a promising probe for the study of quasar outflows. Features that can be used as diagnostics include:

- 1) Appearance of relatively unblended absorption features from both components of the Mg II doublet allows us to determine whether the flow completely covers the emission region. A partial covering of the source is taken as a direct evidence for the intrinsic nature of the absorber (Barlow 1997; Hamann et al. 1997; Arav et al. 1999b), that is, an outflow associated with the AGN. It also shows that the apparent column densities extracted from the absorption trough are only lower limits (Arav 1997; Arav et al. 1999b).
- 2) Neutral helium absorption lines from the highly meta-stable level 2^3S . Very few AGNs

show these lines, where known examples are Mrk 231 (Boksenberg et al 1977; Rudy, Stocke & Foltz 1985), NGC 4151 (Anderson 1974) and perhaps 3CR 68.1 (Brotherton et al. 1998). The He I lines are important diagnostics for the ionization state of the gas. From the ionization equilibrium of this level we can infer lower limits on the He⁺ column density and therefore lower limits on the H II column density. The different oscillator strengths of the detected lines allow us to determine the real optical depth and covering factor of the He I absorbers.

- 3) Detection of absorption from excited states of Fe II allows for lower limits and sometimes even determination of the number density of electrons (n_e) in the gas. In a study of QSO 1044+3656 (de Kool et al. 2000) we were able to determine n_e in the outflow and combined with photo-ionization constraints showed that the outflow is situated about 1000 pc. from the central source.
- 4) Appearance of Mg I absorption necessitates a low ionization parameter, since it is difficult to shield Mg I from ionizing photons. (The ionization parameter U is defined as the ratio of number densities between hydrogen ionizing photons and hydrogen nuclei in all forms.)

To realize this diagnostic potential we observed the optical spectrum of QSO 2359–1241 using the HIRES spectrograph on the Keck telescope. In this paper we concentrate on a detailed analysis of the numerous absorption features seen in our high-resolution ground-based spectroscopic data (§ 2), and in low-resolution HST UV prism data (§ 3). In § 4 we analyze the ionization equilibrium and abundances of the outflow. The discovery of the object, its radio, polarization, and overall optical characteristics are described in a companion paper (Brotherton et al. 2000).

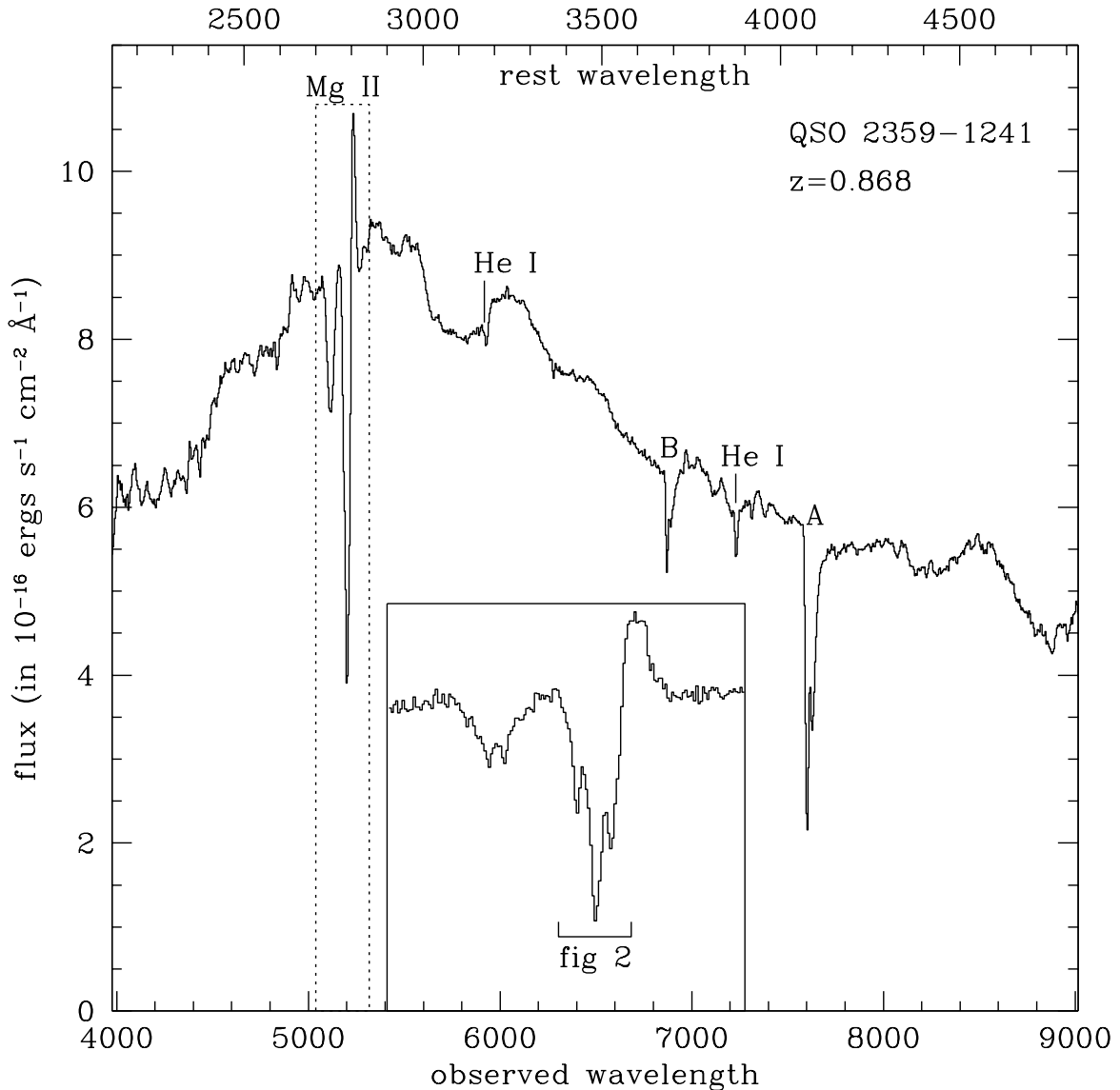


Fig. 1.— Low resolution Keck spectrum with major absorption features marked. An expanded view of the Mg II region is shown in the insert, which covers the spectral interval bounded by the dotted rectangle. The data shown in the insert is from a somewhat higher resolution observation done at Lick. For comparison, figure 2 shows Keck-HIRES data covering only the marked spectral region within the insert.

2. INTRINSIC ABSORPTION IN THE KECK HIRES SPECTRUM

2.1. Data Acquisition and Reduction

On December 26, 1998 we used the High Resolution Echelle Spectrometer (HIRES, Vogt et al. 1994) on the Keck I 10-m telescope to obtain 4×1500 second exposures of QSO 2359–1241 covering $4330 - 7450\text{\AA}$ using a $1''.1$ wide slit. The orders overlap up to 6410\AA , beyond which small gaps occur between orders. The slit was rotated to the parallactic angle to minimize losses due to differential atmospheric refraction. The observing conditions were excellent with sub-arcsecond seeing and near-photometric skies. The spectra were extracted using routines tailored for HIRES (Barlow 2000). The resolution of the final spectrum is $R = 39000$.

A smooth continuum was fit to the spectrum in regions free of absorption or emission features. This procedure is somewhat subjective, particularly in the case of blended emission lines (such as Fe II). While unlikely to create any false absorption features, this normalization introduces some uncertainty in the true continuum level; consequently, equivalent widths of absorption features are somewhat uncertain.

2.2. Intrinsic Nature of the Absorption

Many of the absorption features in the HIRES data arise from a complex intrinsic absorber. The evidence for the absorber being intrinsic is based on: 1) Comparing the absorption features seen in the Mg II doublet (the apparent optical depth ratio differs from the nominal value of 1:2). 2) Existence of He I absorption from a meta-stable state, which requires the density of the absorber to be several orders of magnitude larger than is seen in the ISM and IGM. 3) Existence of Fe II absorption from excited levels, which also necessitates high density. 4) Appearance of full fledge BALs (C IV $\lambda 1549$, Si IV $\lambda 1397$) in the HST FOC spectrum which coincide in velocity with the absorption seen in the HIRES data. Each of these separate pieces of evidence is enough by itself to identify the absorption system as intrinsic. In the rest of this section we analyze the features in the HIRES data that are associated with this intrinsic absorber.

2.3. Mg II

A high resolution spectrum of the Mg II absorption feature reveals a rich and complex structure. In figure 2 we show HIRES data for a part of the Mg II absorption, the spectral region shown in figure 2 is marked on the insert to figure 1. We have labeled five distinct absorption features (*a* – *e*) associated with the red doublet component, which are also seen in the blue doublet component. Absorption features *f* and *g* are seen in the blue doublet

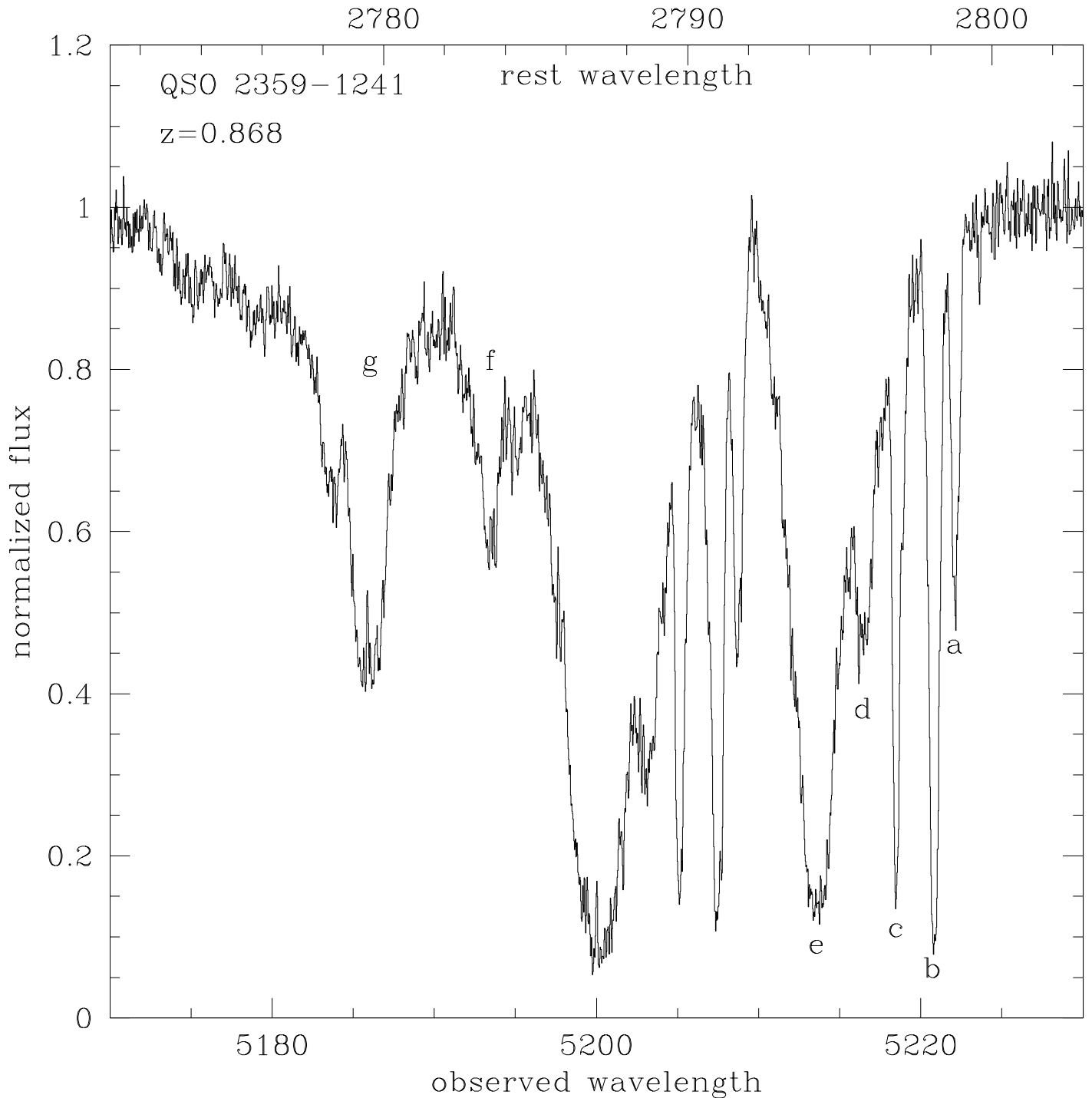


Fig. 2.— Normalized HIRES data (see text) of the Mg II absorber. Individual features are marked: *a* – *e* in the red doublet component, *f* and *g* in the blue doublet component. The spectral coverage of this plot is marked in the insert to Fig. 1.

component, but their red counterparts are blended with the $(a - e)$ blue complex.

The appearance of the same features in both doublet components allow us to study the covering factor and real optical depth of the outflow. However, the situation in QSO 2359–1241 is not ideal since the red component of feature g falls in the middle of blue component of feature e ; the red component of feature f contaminates the blue component of feature b ; and there is a shallower red absorption contribution across the entire blue absorption structure $a - e$. These contaminations do not allow for a clean simultaneous solution for the covering factor and the optical depth (as was done for the Si IV BAL in QSO 1603+3002; Arav et al 1999b). However, most of the contaminating absorption is rather shallow and we can still get semi-quantitative results from analyzing the relationship between the same absorption features seen in both doublet components.

To analyze the residual intensities we first need to normalize the data. Since the absorption occur on the blue wing of the Mg II broad emission line (BEL), there are two physical choices here. First, the outflow may cover both the continuum source and the BEL region. In this case we model the emission line with two Gaussians and divide the data by the assumed unabsorbed emission, which consists of the BEL plus continuum. Second, the outflow may only cover the continuum source and not the BEL region. In BALQSO 1603+3002 there is strong evidence that the flow does not cover the BELs (Arav et al 1999b). For this case we need to subtract the modeled BEL from the data in order to determine the flux seen by the absorber. We then divide this flux by the continuum to obtain the normalized flux seen by the absorber. We will argue below that the second scenario is more probable and use this normalization in figure 2.

Figure 3 shows a comparison of the Mg II absorption features in each doublet component. For direct comparison we use velocity presentation and the two panels show the two normalizations discussed above. We use a thick solid line for the blue component data and a thin line for the red one. If the flow fully covers the QSO’s emission (both continuum source and BEL regions), the expected residual intensity of the absorption features seen in the blue doublet component is: $I_b(v)[\text{expected}] = I_r^2(v)[\text{observed}]$; where I_r is the residual intensity of the absorption features seen in the red doublet component. We plot this expected blue residual intensity in figure 3 as a dotted line. In both normalizations it is evident that the depth of features a, b and c in the blue doublet component is smaller than expected by assuming complete coverage. This is a clear indication for partial covering and hence for the intrinsic nature of the absorption (Barlow 1997). We note that partial covering is not restricted only to geometrical coverage. The photons at the bottom of the troughs may also arise from scattering contribution. If we assume that the flow does not cover the BEL region, the top panel in figure 3 show that the residual intensities for features b and c are identical within the errors in both doublet components. In this case both features are saturated ($\tau_{\text{red}} \gtrsim 3$) and the shape of the absorption profile is completely dependent on the covering factor. If the flow covers the continuum and the BEL equally,

then from the bottom panel of figure 3 we also infer that the blue doublet absorption of features a, b and c is not deep enough if we assume complete coverage. Therefore, we conclude that no matter which normalization we use the flow in features a, b and c show partial coverage and hence demonstrate the intrinsic nature of the absorber.

Which of the two covering scenarios is more probable? In the case of BALQSO 1603+3002 we argued that “in the absence of a physical preference for τ_{real} values of order unity, values between 2–5 necessitate some fine tuning whereas the range $5 - \infty$ is simply much more probable numerically.” This argument suggests that it is more probable that features b and c do not cover the BEL region. However, we notice that the equal covering normalization (bottom panel in Fig. 3) shows that feature d might completely cover both the continuum source and the BEL region (expected and observed blue component are equal). This scenario is simpler, since it does not necessitate a partial covering factor, and thus is more appealing. We suggest that the first argument is somewhat stronger and therefore it is more probable that features b and c do not cover the BEL region. However, the evidence is weaker than is seen in BALQSO 1603+3002.

In addition to components $a - g$ there is a high velocity trough at -5000 km s^{-1} , which can be seen in the insert to figure 1. We do not show the HIRES data since they do not reveal qualitatively different structure than the one seen in the insert. A Mg II doublet structure is evident in the feature and the HIRES data confirm that the depth ratio of the two components is 1:1, that is, complete saturation. This 1:1 depth ratio is caused by partial covering factor, which indicates that the absorption system is intrinsic.

2.4. Apparent Column Densities

In Table 1 we give the apparent column density measurements of the intrinsic absorption features for all the identified lines. Apparent column density are derived by substituting the apparent optical depths of the troughs (defined as $\tau = -\ln(I_r)$, where I_r is the normalized residual intensity seen in the trough) in:

$$N_{\text{ion}} = \frac{3.7679 \times 10^{14} \text{ cm}^{-2}}{\lambda_0 f_{ik}} \int \tau(v) dv, \quad (1)$$

where λ_0 and f_{ik} are the transition’s wavelength and oscillator strength, and where the velocity is measured in km s^{-1} . We note that the apparent column densities give good estimates for the real column densities only if the absorbing material covers the emission source completely and uniformly and where scattered-photons do not contribute appreciably to the residual intensity in the troughs (see discussions in Korista et al 1992; Arav 1997). Otherwise, apparent column densities are only lower limits on the real ones (Arav et al 1999a, Arav et al 1999b). We define $gf\lambda$ (where g is the statistical weight, f is the oscillator strength and λ is the transition’s wavelengths) as the strength factor of the

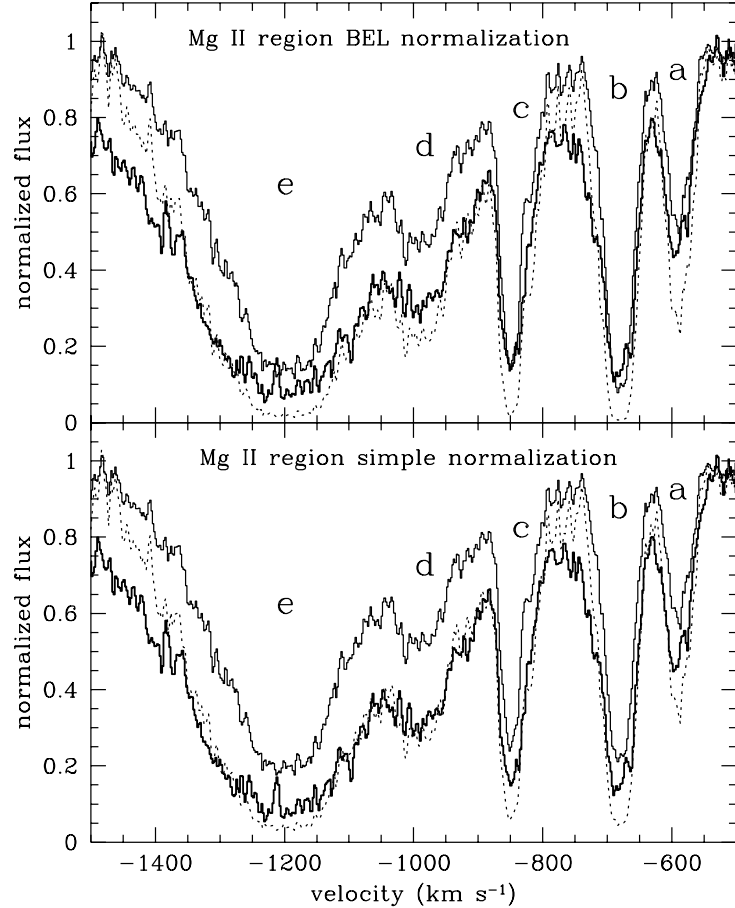


Fig. 3.— Mg II absorption data in two different normalizations. Bottom panel shows simple normalization, data divided by the sum of modeled continuum and modeled BEL. The thick solid line shows the data for the blue doublet component; the thin solid line indicates the red doublet component; the dotted line shows the expected blue doublet absorption given the red component data. Top panel shows the same for the case where we assume the absorption covers the continuum region but not the BEL region. This is done by subtracting a modeled BEL from the data and dividing the result by the continuum.

line and give its value (normalized to that of the strongest transition; data from Verner, Verner & Ferland 1996). For the Fe II lines we multiplied the expression in equation (1) by the ratio of statistical weight of the lower level (summed over all observed states) to that of the specific state. This procedure yields independent estimates for $N_{\text{Fe II}}$ from each transition provided the level populations are in LTE.(see § 2.6). In Mg II components c and d are embedded in a wide extension of component e , their integration interval only covers the regions where these feature are distinctive, without compensation for the fact that some of the absorption is due to the wing of component e . For the other lines the different absorption components are well separated, and therefore the integration over the components is straightforward. For the He I measurements we corrected for the atmospheric absorption seen in the spectral region around the intrinsic He I $\lambda 3890$ line (especially evident on the red side of component e , see Fig. 4). The estimated error for each line is derived by performing the integration given in equation (1) on two absorption free regions in the spectral vicinity of the measured features and taking the average of their absolute values. This procedure takes into account both signal-to-noise and continuum uncertainties. The error is formally derived for component e and can be used as a conservative estimate for the other components since they are narrower. For Mg II the error is significantly larger since we had to take the blending of the different components into account.

TABLE 1: HIRES APPARENT IONIC COLUMN DENSITIES

| Ion | Transition | Strength ^a | N(e) ^b | N(d) ^b | N(c) ^b | N(b) ^b | N(a) ^b | error ^c | N(tot) ^b |
|-------|---------------------|-----------------------|-------------------|-------------------|-------------------|-------------------|-------------------|--------------------|---------------------|
| (1) | (2) | (3) | (4) | (5) | (6) | (7) | (8) | (9) | (10) |
| Ca II | 3970 | 1 | 12.43 | 11.06 | 11.68 | 11.59 | 10.90 | 11.1 | 12.57 |
| He I | 3889 | 1 | 13.80 | 12.70 | 13.14 | 13.19 | 12.76 | 12.3 | 14.02 |
| He I | 3189 | .36 | 13.85 | 12.29 | 12.22 | 12.94 | 12.49 | 12.8 | 13.90 |
| He I | 2946 | .17 | 13.87 | 12.47 | 12.96 | 13.30 | 12.82 | 13.0 | 14.00 |
| Mg I | 2853 | 1 | 11.88 | 10.98 | 11.44 | 11.53 | 10.68 | 10.7 | 12.18 |
| Mg II | 2803 | 1 ^d | 14.21 | 13.21 | 13.30 | 13.38 | 12.89 | 12.6 | 14.43 ^e |
| Fe II | 2632*, ^f | 0.46 | 13.59 | 12.84 | 11.45 | 12.25 | 12.32 | 12.6 | 13.65 |
| Fe II | 2612* | 0.33 | 13.65 | 13.13 | 13.09 | 11.77 | 12.50 | 12.8 | 13.83 |
| Fe II | 2608* | 0.22 | 13.83 | 12.35 | 13.02 | 12.87 | 13.10 | 13.1 | 14.00 |
| Fe II | 2600 | 0.76 | 13.66 | 12.83 | 12.76 | 12.91 | 12.14 | 12.5 | 13.83 |
| Fe II | 2587 | 0.17 | 13.92 | 12.56 | 13.47 | 13.30 | 12.88 | 13.1 | 14.16 |
| Fe II | 2405.6* | 0.43 | 13.63 | 12.37 | 12.74 | 13.00 | 12.01 | 13.0 | 13.61 |
| Fe II | 2396.4* | 0.68 | 13.62 | 12.11 | 11.42 | 13.08 | 11.80 | 12.8 | 13.73 |
| Fe II | 2382 | 1.00 | 13.61 | 12.67 | 12.71 | 12.87 | 12.75 | 12.6 | 13.81 |

^a - Expected absorption strength ratio for lines from the same ion (essentially normalized $gf\lambda$, see text).

^b - \log_{10} of the column density for each absorption subcomponent (see Figs. 4 and 5).

^c - Also in units \log_{10} of the column density. The error is roughly appropriate for each individual component, and takes into account both signal-to-noise and continuum uncertainties.

^d - Although the red doublet component of Mg II is only as strong as the blue one, we give it strength=1 since we do not report the blue component measurements separately.

^e - Total column density for Mg II includes contributions from component *f* ($\log(N) = 13.41$) and *g* ($\log(N) = 13.06$), which are associated with the blue component of the Mg II doublet.

* - Transition from excited level.

^f - A blend of two excited transitions Fe II $\lambda 2632.11$ and Fe II $\lambda 2631.83$.

2.5. He I

Figure 4 shows absorption in He I, Mg I and Ca II associated with the intrinsic absorber. All the lines are plotted on the same velocity scale where the wavelength of the transition in the rest frame of the object is at 0 km s⁻¹. The spectral segments are plotted in the same normalized flux scale which is shifted for each line for presentation purposes. Absorption features from the He triplet lines are easily recognized as being part of the intrinsic outflow. The column densities for the three He I lines in each feature are in agreement given the errors, implying that unlike the Mg II case the He I absorption is not saturated. This finding is a prerequisite for determining the ionization equilibrium and abundances in the flow (see § 4), since it gives us the actual column density as opposed to a lower limit available from the apparent column density.

The observed He I lines all arise from the meta-stable level 2³S. Extensive treatment of this level appears in the literature and the following discussion is largely based on: Macalpine (1976); Rudy, Stocke, & Foltz (1985); Clegg (1987); Oudmaijer, Busfield, & Drew (1997), all of which rely to some extent on Osterbrock's "Astrophysics of Gaseous Nebulae" (1974). In equilibrium, the population of the 2³S is determined by the balance of arrivals from recombination to all triplet levels versus departures mainly due to collisional transition to other levels. Since under most conditions all recombinations to the triplet levels end up in the 2³S level we obtain:

$$n_{He^+} n_e \alpha_T = n_{2^3S} \left[A_{21} + n_e (q_{tr} + q_{ci}) + \int_{\nu_0}^{\infty} \frac{a_{\nu} L_{\nu}}{4\pi r^2 h \nu} d_{\nu} \right], \quad (2)$$

where n_{He^+} is the number density of singly ionized helium, n_e is the electron number density, α_T is the total recombination coefficient to all triplet levels, n_{2^3S} is the number density of neutral helium in the 2³S level, A_{21} is the Einstein A coefficient for the forbidden transition (625 Å) from the 2³S level to the ground level (1¹S), q_{tr} is the rate of collisional transfer to all singlet level (which is dominated by collisions to the 2¹S and 2¹P levels), q_{ci} is the collisional ionization rate which becomes important above 20,000 K (Clegg 1987), a_{ν} is the photoionization cross section for 2³S, $L_{\nu}/(4\pi r^2 h \nu)$ is the flux of ionizing photons (L_{ν} is the luminosity per unit frequency, r is the distance to the emitting source and h is Planck's constant), ν_0 is the threshold frequency for ionizing the 2³S level (4.77 eV, 2600 Å).

Equation (2) can give us a maximum for the n_{He^+}/n_{2^3S} ratio. Neglecting photoionization, collisional ionization and radiative transition to the ground level (i.e., assuming n_e larger than the critical density of 3×10^3 cm⁻³) we obtain: $n_{He^+}/n_{2^3S} = \alpha_T/q_{tr}$ Using the values given for α_T and q_{tr} given in Clegg (1987) and Osterbrock (1974) we find $n_{2^3S}/n_{He^+} = 6 \times 10^{-6}$ More generally, Clegg (1987) gives the above ratio as function of n_e and temperature (including radiative transition to the ground level but neglecting photoionization) as:

$$\frac{n_{2^3S}}{n_{He^+}} = \frac{5.8 \times 10^{-6} T_4^{-1.19}}{1 + 3110 T_4^{-0.51} n_e^{-1}} \quad (3)$$

where T_4 is the temperature in units of 10^4 K. Equation (3) is a good approximation for $8,000 < T < 20,000$, where in our case the temperature might be somewhat lower (see below). We can use these estimates combined with our measurement for the total column density seen in the He I metastable lines, to set a minimal He⁺ column density of $\sim 2 \times 10^{19}$ cm⁻² in the intrinsic absorber. Assuming solar abundances this estimate yields a minimal H II column density of $\sim 2 \times 10^{20}$ cm⁻².

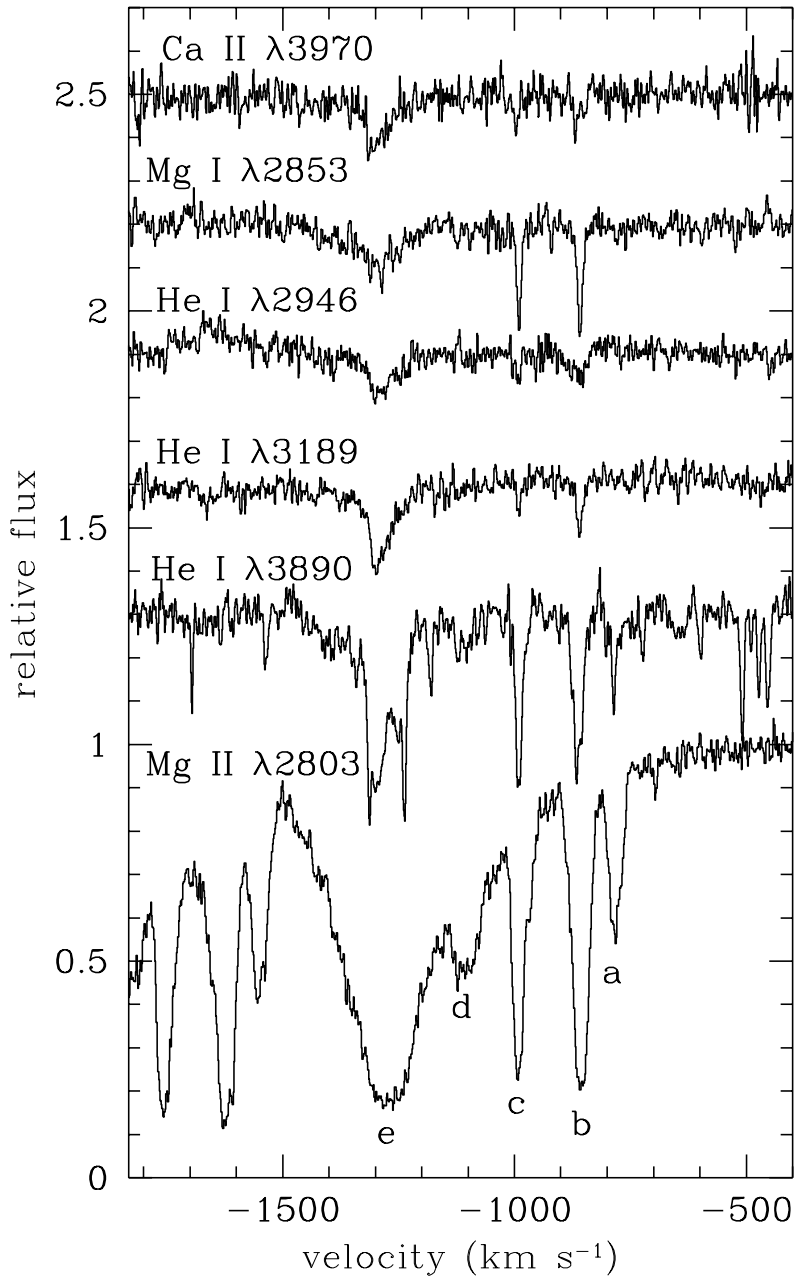


Fig. 4.— Absorption troughs from three He I lines, Ca II $\lambda 3970$ and Mg I $\lambda 2853$ are plotted on the same velocity scale together with the intrinsic absorption seen in Mg II. The sub-troughs are labeled underneath the Mg II data.

2.6. Fe II

Many Fe II absorption features are detected in the HIRES data. In table 1 we give column density measurements for the most unambiguous detections and in figure 5 we plot the absorption associated with five of these on the same velocity scale of the absorption seen in Mg II $\lambda 2803$ line. The S/N of the Fe II features is lower than that of the magnesium and He I features due to the lower throughput of the HIRES detector at shorter wavelengths. For this reason we concentrate our discussion on feature *e* which is the strongest one detected in all the lines.

Absorption features from excited levels of Fe II are clearly detected. These transitions arise from energy levels 0.05 eV. ($\lambda 2612, \lambda 2396.4$) and 0.08 eV. ($\lambda 2608, \lambda 2405.6$) above ground. Transitions from two slightly higher energy levels are also detected (0.11 and 0.12 eV.), although we do not include them in the table since their detection significance is lower. The $N_{\text{Fe II}}$ values given in table 1 assume LTE population of the levels at the limit $kT \gg \Delta E$ (where k is Boltzmann’s constant, T is the temperature and ΔE is the energy difference between the levels). That is, the ratio of optical depth of two features is given by:

$$\frac{\tau_1}{\tau_2} = \frac{n_1 f_1 \lambda_1}{n_2 f_2 \lambda_2} = \frac{g_1 f_1 \lambda_1}{g_2 f_2 \lambda_2}, \quad (4)$$

where n_1 and n_2 are the level populations of lower level that give rise to each transition; λ_1 and λ_2 are the transitions’ wavelengths, f_1 and f_2 are the oscillator strengths and g_1 and g_2 are the statistical weights of the levels. For the last equality we used the assumption of LTE population at the limit $kT \gg \Delta E$. We define $gf\lambda$ as the strength factor of the line and give its value (normalized to that of the strongest transition; data from Verner, Verner & Ferland 1996) in table 1. Six of the lines (from both ground and excited states) give consistent estimates for $N_{\text{Fe II}}$, validating the LTE assumption, and like the He I case show that the inferred $N_{\text{Fe II}}$ are actual determinations and not lower limits. The two inconsistent $N_{\text{Fe II}}$ estimates are probably due to uncertainties in the oscillator strength of these transitions (see de Kool et al. 2000).

Since the highest energy level we detect (0.12 eV.) is equivalent to a temperature of ~ 1000 K, we infer that the absorbing gas is at $T \gtrsim 2000$ K. Lower temperature will cause a significant reduction in the higher level population due to the exponential factor in the Boltzmann equation, and this is not seen in the data. We are also able to constrain the temperature from above due to the non-detection of Fe II $\lambda 2563$, which arise from a 1.0 eV. level. In order to suppress the 1.0 eV. level population below our detection limit we must have $T \lesssim 10,000$ K. The detection of Fe II excited transitions necessitates the gas to be above the critical density for these transitions. From this we infer $n_e \gtrsim 10^5 \text{ cm}^{-3}$ (see de Kool et al. 2000). Finally, the non detection of Fe I $\lambda 2524$ necessitate $\log(U) > -5$. Photoionization models (see § 4) show that at smaller values of U we should have detected an appreciable absorption in the Fe I line given the inferred Fe II column density (see Fig. 7).

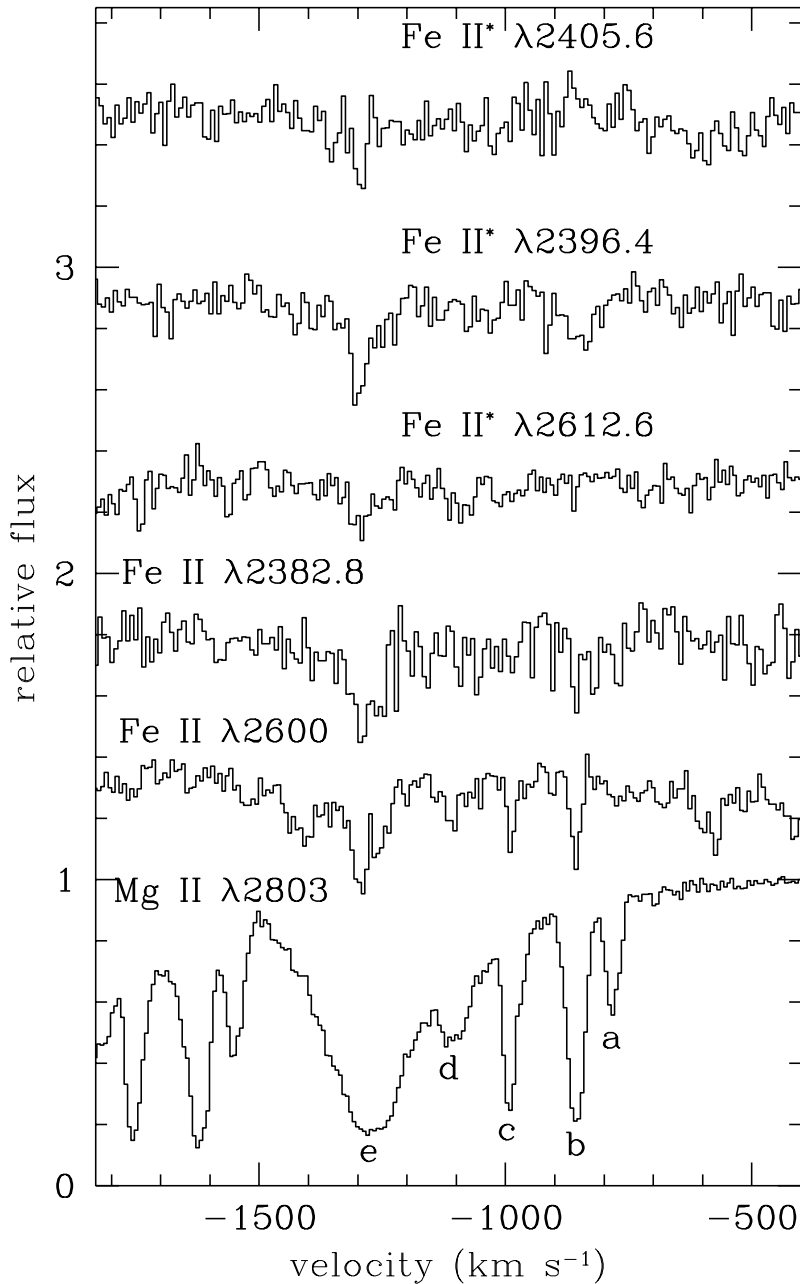


Fig. 5.— Similar to Fig. 4 for five Fe II transitions, two of which are from excited states. Data smoothed by four pixels to compensate for lower signal-to-noise at the blue end of the HIRES spectral coverage.

2.7. Mg I and Ca II

In figure 4 we identify components *b*, *c* and *e* in Mg I λ 2853. A detection of this line is significant since the ionization potential of the ion is 7.6 eV. As discussed in de Kool et al. (2000), this low ionization energy does not allow a hydrogen ionization front to protect the Mg I ions from destruction by shielding it from ionizing photon. This is in contrast to the case of Mg II with ionization potential of 15.0 eV, which is higher than that of hydrogen (13.6 eV). Therefore, a hydrogen ionization front can protect the Mg II ions from photodissociation (Voit, Weymann & Korista 1993). Since shielding does not work for Mg I a low ionization parameter is needed in order for it to survive in the typical radiation environment produced by the quasar. We discuss this issue further in § 4.

Components *b* and *c* are most prominent in Mg I. This gives independent support to the conclusion from the Mg II analysis that components *b* and *c* have larger optical depth compared to the other components. In Mg I we do not detect components *a* and *d*. Using the upper limits for *a* and *d* we conclude that τ_b and τ_c are at least five times larger than τ_a and τ_d . Our spectral coverage also contains the red component of the Ca II doublet (λ 3970). The line is clearly detected in component *e* and marginally detected in components *b* and *c*.

3. HST FOC SPECTRUM

A low-resolution UV spectrum of QSO 2359–1241 was obtained using the Faint Object Camera (FOC) on-board the HST. The data reduction and characteristics are described in Brotherton et al (2000). Figure 6 shows part of the FOC spectrum. Two deep and wide absorption features are seen in the spectrum. These are C IV λ 1549 and Si IV λ 1397 BALs from the same system. Several additional absorption features are also noticeable. We use the Mg II absorption template to determine the relationship between the absorption features seen in the FOC data to those seen in the ground-based observations. To identify FOC absorption features associated with the Mg II absorption, we displace the Mg II template to the expected wavelength position of a candidate transition. This is done by multiplying the rest wavelength of the template by $\lambda_c/\lambda_{\text{Mg II}}$, where λ_c is the wavelength of the candidate transition. The result (shown in figure 6) confirms the existence of absorption features from the resonance lines Al III λ 1857, C IV λ 1549, Si IV λ 1397, and N V λ 1240 associated with the Mg II intrinsic absorption. We also note that the steep intensity drop on the red wing of the Ly α BEL can be explained by a Ly α BAL from the same system.

As evident from figure 6, there are differences in the shape of the absorption features in the FOC data to the Mg II template, especially the C IV feature. Some of these are caused by the much lower resolution of the FOC spectrum. However, the fact that the Si IV and C IV absorption features are more extensive than can be extrapolated from the Mg II template is not unique. QSO 0059–2735 shows a similar behavior (Weymann et al 1991,

Wampler, Chugai & Petitjean 1995), where the Si IV and C IV BALs are much wider than the Mg II BAL. In table 2 we give apparent column densities for the BALs seen in the FOC spectrum. A comparison with table 1 shows that the apparent column density of Al III is similar to that of Mg II, a phenomenon that is also observed in QSO 0059–2735 (Weymann et al. 1991, Wampler, Chugai & Petitjean 1995) and in QSO 1232+1325 (Voit, Weymann & Korista 1993). In contrast, the apparent column density of the C IV and Si IV BALs are roughly an order of magnitude larger than the Mg II BAL, which is a consequence of the much larger width of the Si IV and C IV BALs. Again this is similar to what is observed in QSOs 0059–2735 and 1232+1325. We elaborate further on the relationship between the high and low ionization absorbers in the discussion.

In summary, the FOC spectrum shows the following BALs associated with the Mg II intrinsic absorption: Al III λ 1857, C IV λ 1549, Si IV λ 1397, and N V λ 1240. The low resolution of the FOC spectrum does not allow for much analysis of these BALs, other than the fact that the C IV λ 1549, Si IV λ 1397 are full fledged BALs with a full-width-half-maximum of ~ 8000 km s $^{-1}$.

TABLE 2: FOC APPARENT IONIC COLUMN DENSITIES

| Ion (1) | Transition (Å) (2) | log(N _{ion}) (3) |
|------------|-----------------------|-------------------------------|
| Al III | 1857 | 14.0±0.15 |
| C IV | 1549 | 15.7±0.1 |
| Si IV | 1397 | 15.4±0.1 |
| N V | 1240 | 15.2±0.1 |

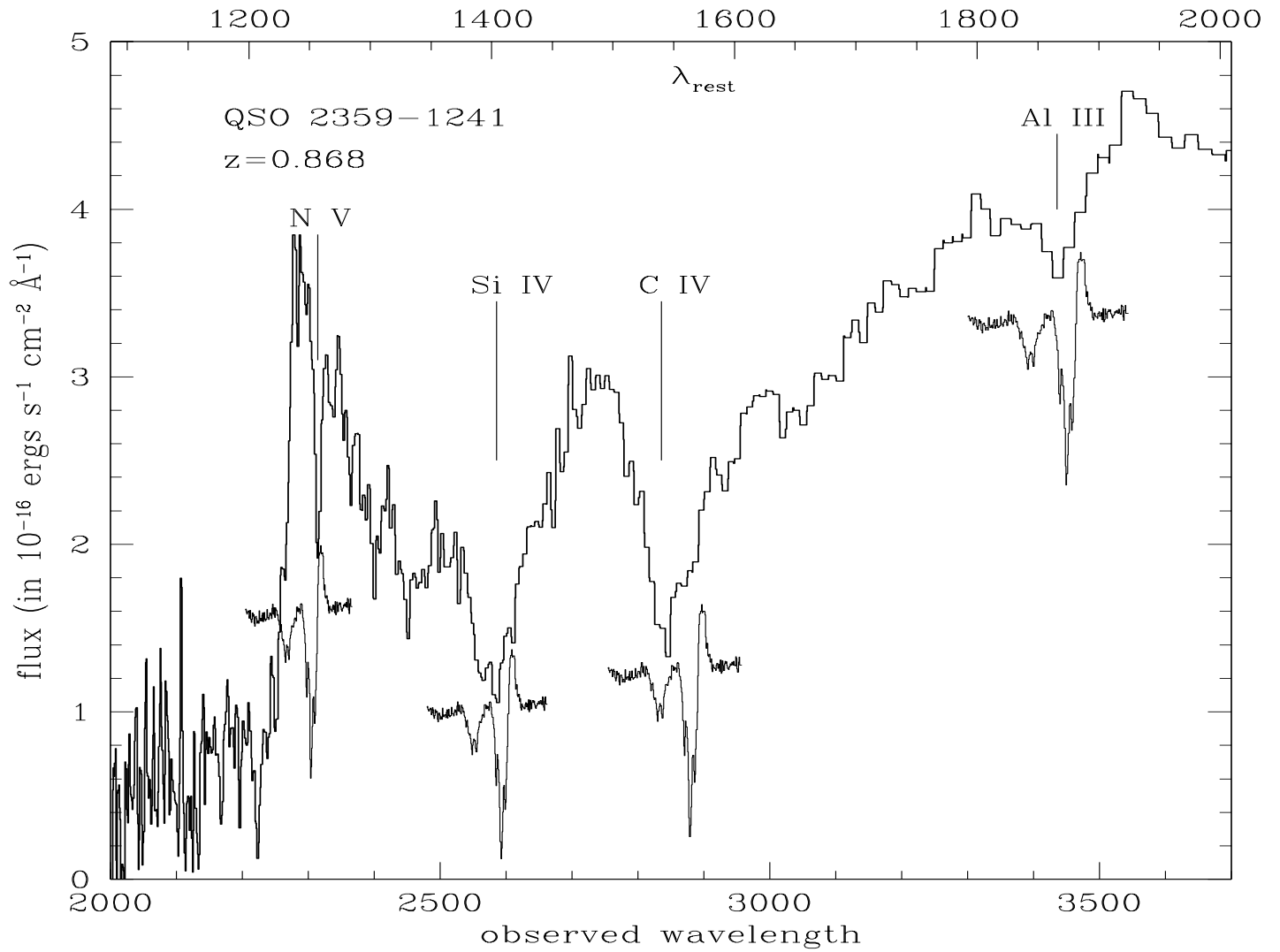


Fig. 6.— Portion of the FOC spectrum with main absorption features labeled. These are identified using the Mg II ground-based template (see text). Good matches are seen for intrinsic absorption in: Al III $\lambda 1857$, C IV $\lambda 1549$, Si IV $\lambda 1397$ and N V $\lambda 1240$.

4. IONIZATION EQUILIBRIUM AND ABUNDANCES

In § 2 we established that the He I and Fe II absorption features are not saturated, therefore their apparent column density measurements are the actual column densities of the absorber and not just lower limits. The importance of this verification can hardly be overstated. Unless we have a direct evidence that a specific absorption trough in a quasar’s outflow is not saturated, we must assume that it is, since in most cases where saturation diagnostics exist, we find that the troughs are indeed saturated (Arav 1997; Telfer et al. 1998; Arav et al. 1999a; Churchill et al. 1999; Arav et al. 1999b; De Kool et al. 2000). In these cases, using the apparent column densities as real ones undermine the ionization equilibrium and abundances results inferred from ionization models, since the output of these models are the real column densities.

4.1. Optically Thin Models

We begin by examining photoionization models that are optically thin in the Lyman limit ($\tau_{LL} \ll 1$). The output we are most interested in are the ionic column densities (N_{ion}), These depend strongly on the input ionization parameter (U), total hydrogen column density (N_H) and metalicity. To a lesser extent N_{ion} also depend on the shape of the incident continuum and are relatively insensitive to variation of n_H in the range 10^5 cm $^{-3}$ (our lower limit based on the Fe II troughs) to 10^{10} cm $^{-3}$ (the estimated density in the broad emission line region). With all other parameters fixed, N_{ion} depends linearly on N_H , the atoms become more ionized with the increase of U and a higher metalicity correlates linearly with higher N_{ion} for the metals. In all our models we assume solar metalicity. The elimination of this degree of freedom naturally tightens the constraints we derive for the ionization equilibrium. As we show below, models based on solar metalicity can satisfactorily reproduce the observed N_{ion} . For the incident spectrum we used AGN continua given in the photoionization package CLOUDY (Ferland et al. 1996): Table AGN, which is essentially the Mathews and Ferland spectrum (Mathews and Ferland 1987) and two variants of a superposition of a black body and various power laws. We found that the result are only moderately dependent on which of the three input continua is used (see § 4.3) and therefore we concentrate on results obtained using the Table AGN continuum.

Figure 7 shows the relative N_{ion} as a function of U for most of the ions we detect in the HIRES spectrum. The most important constraint arise from comparing the prediction and measurement for the ratio $N_{Fe\,II}/N_{He\,I^*}$ (where He I* designate He I in the 2^3S metastable level). When Fe II is the dominant iron ion, we expect $N_{Fe\,II}/N_{He\,I^*}$ to be between 30–100 since the solar abundance of iron is 3.2×10^{-5} relative to hydrogen whereas that of the He I* is only $\sim 6 \times 10^{-7}$ (based on eq. 3, assuming most helium is in He II and using helium abundance of 10% relative to hydrogen; we note that the temperature of the models ranges

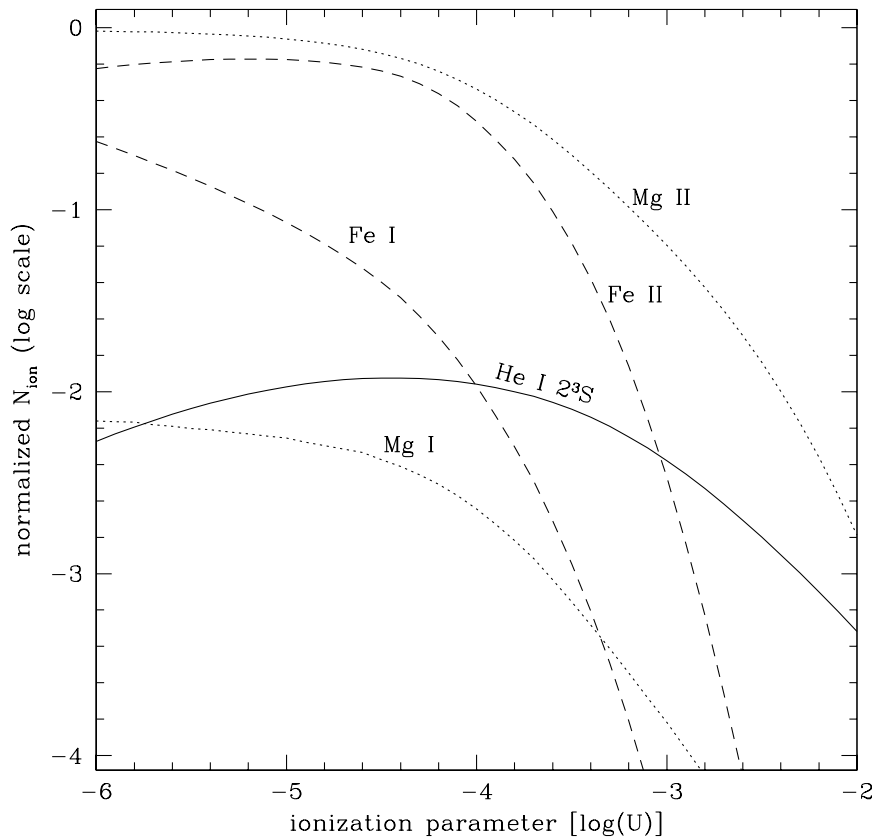


Fig. 7.— Optically thin ionization models ($\tau_{LL} \ll 1$), using the “table agn” continuum with $n_H = 10^8 \text{ cm}^{-3}$. The ionic column densities are normalized to the total magnesium column density.

from 8000 K to 20,000 for $\log(U)$ between -6 and -2 , respectively). Since the observed N_{HeI^*} is somewhat larger than N_{FeII} we conclude that Fe II cannot be the dominant iron ion. From figure 7 we deduce that the observed N_{FeII}/N_{HeI^*} exclude models with $\log(U) < -3.5$. Furthermore, the considerable difference in the slopes of N_{FeII} and N_{HeI^*} allows for only a narrow range around $\log(U) = -3$ for acceptable models.

What about the other observed ions? The magnesium column densities fits very well into the above picture. Comparing the measurements in table 1 to the models in figure 7 we note that the observed N_{MgI}/N_{HeI^*} can be reproduced by the models only in a narrow range of $\log(U) \gtrsim -3$. The modeled N_{MgII} are consistent with this picture since the measurements are only lower limits (see § 2.3). For Ca II we also get consistent results and the upper limit for N_{FeI}/N_{FeII} is readily satisfied as long as $\log(U) > -5$, while the upper limit for N_{FeI}/N_{HeI^*} necessitates $\log(U) > -3.5$

4.2. Models with a Hydrogen Ionization Front

Although optically thin models can produce all the observed N_{ion} ratios, they have difficulties in explaining some of the measured column densities themselves, especially N_{HeI^*} . For $\log(U) = -3$, figure 7 shows that $N_{Mg}/N_{HeI^*} \simeq 250$, or using solar abundances $N_H/N_{HeI^*} \simeq 7 \times 10^6$. Therefore, in order to produce the observed $N_{HeI^*} = 6 \times 10^{13} \text{ cm}^{-2}$ we need a total $N_H = 4 \times 10^{20} \text{ cm}^{-2}$. This amount of N_H produces a strong hydrogen ionization front (i.e., a region where the dominant hydrogen ion shifts from H II to H I) with $\tau_{LL} > 1000$ for $\log(U) = -3$, thus invalidating our optically thin assumption. Moreover, models with such a thick hydrogen ionization front cannot produce the observed N_{ion} either. For the specific example above, the predicted N_{FeII}/N_{HeI^*} is more than 100 times the observed one.

Figure 8 illustrates the situation for models with a hydrogen ionization front. Prior to the development of the hydrogen ionization front, the relative column densities are similar to the ones in the optically thin models. We chose to present a model with $\log(U) = -3$ since the predicted ratio N_{FeII}/N_{HeI^*} agreed with the observed one in the optically thin part. Behind the front the situation changes radically. The appearance of lines from the He I 2^3S metastable level requires a significant fraction of He II in the gas. However, in close proximity to the H I ionization front we find a He I ionization front making He I the dominant helium species. Therefore, the fraction of He II behind a hydrogen ionization front decreases sharply and with it that of He I* (see eq.(3)). We note that the increase in the relative fraction of He I* in the vicinity of the front is mainly due to the helium ionization transition. For optically thin models with $\log(U) = -3$ the more abundant helium ion is He III (although only by a factor 1.4 compared to He II). As the equilibrium shifts towards He I, at some point He II becomes most abundant, which causes the abundance peak for the He I*. As explained above, at a higher column density He I become the dominant species accompanied by a sharp decline in the He II fraction and hence in that of He I*.

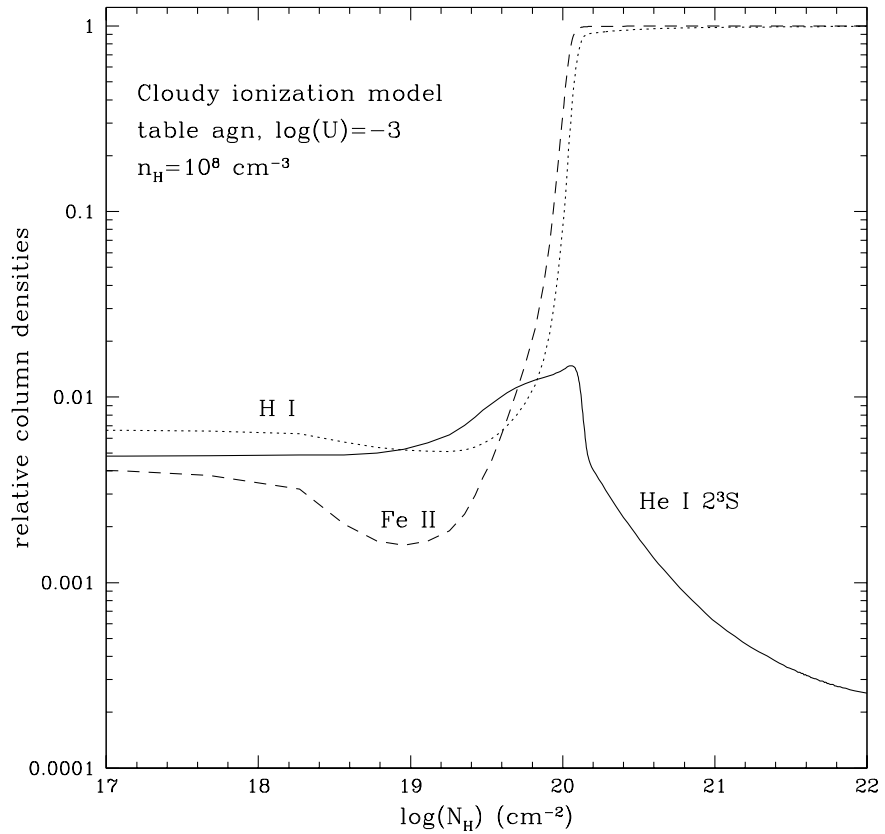


Fig. 8.— Photoionization model with a strong hydrogen ionization front. The Fe II and He I curves are normalized to the total iron column density (assuming solar abundances). The H I curve is normalized to the total N_H .

For the Fe II lines the situation is quite the opposite. A hydrogen ionization front protects the Fe II ions from photoionization and thus making it the dominant species. As a result, almost all the iron behind the front is in the form of Fe II. In the example given in figure 8 the relative fraction of Fe II increases by a factor of 300 across the front, whereas the fraction of He II and with it that of He I* decreases sharply behind the front. Regardless to the U value of the incident spectrum, a strong hydrogen ionization front always causes Fe II to be the dominant iron species behind the front. Since even under the most favorable conditions $N_{\text{Fe}}/N_{\text{HeI}^*} \gg 10$ (based on eq. [3], assuming solar abundances and the allowed temperature range discussed in § 2.6), we conclude that models with a hydrogen ionization front cannot reproduce the observed Fe II and He I* column densities simultaneously.

4.3. Realistic Model Fits

From the analysis above we concluded that optically thin models have difficulties in reproducing the observed column densities while models with a hydrogen ionization front fail completely. The obvious thing to try next are models with an intermediate H I optical depth (τ_{LL} of a few). We aim to find models that can yield the observed column densities of component e (see Figs 4 and 5, and table 1) for which we have the most accurate measurements. In doing so we put most weight on the He I and Fe II results since we have direct evidence that the column densities we measure for these two ions are real ones and not lower limits. It is highly probable that the Mg I and Ca II are also not saturated (due to similarities with the Fe II and He I features, as well as their moderate depth), however we do not have direct diagnostics to confirm that.

In figure 9 we show the column density results from three models as well as the observed ones. In order to keep the models simple we used two AGN continua given in the photoionization package CLOUDY (Ferland et al 1996; A full description is given in the “Hazy” document which describes the code and is available at: http://nimbus.pa.uky.edu/cloudy/cloudy_94.htm). The “Table AGN” model is fully determined by the package and is described in detail in Mathews and Ferland (1987). For the model which is a superposition of a black body “big bump” and various power laws, we used two settings: 1) the default parameter choices given in the Hazy document, $T=150,000$ K, $\alpha_{ox} = -1.4$, $\alpha_{uv} = -0.5$, $\alpha_x = -1$; 2) $T=100,000$ K, $\alpha_{ox} = -2$, $\alpha_{uv} = -0.5$, $\alpha_x = -1$, which gives a somewhat lower temperature across the cloud. The average temperature for each model is given in Table 3, where the difference in temperature across each model is less than 15%. As noted above, the column densities are largely insensitive to variation of n_H in the range 10^5 cm^{-3} to 10^{10} cm^{-3} . For the presented models we chose n_H value close to our Fe II-inferred lower limit, since they gave somewhat lower temperatures, in better agreement with the Fe II temperature constraints. The Table AGN and big bump models give excellent fits for the Fe II and He I column densities. The models over-predict N_{MgI} by

about a factor of three and give a reasonable fit for $N_{\text{Ca II}}$. Although we did not include aluminum in figure 9 (since we do not have high-resolution data for it), we note that these models also reproduce the apparent $N_{\text{Al III}}$ (see table 2) to within a factor of two. The low abundance of aluminum ($[\text{Al}/\text{H}]_{\odot} = 3 \times 10^{-6}$) coupled with the inferred N_{H} in the object, suggests a low level of saturation (if any) in the Al III absorption, thus implying that the apparent $N_{\text{Al III}}$ is a reasonable approximation for the actual one.

How does the presence of other flow components affect our ionization analysis? Although the measurements of components $a - d$ are not as accurate, it seems that their column density ratios, and therefore their ionization equilibrium, are similar to that of component e . This situation argues in favor of models with lower τ_{LL} . A moderately strong τ_{LL} ($\gtrsim 4$) in a given component will strongly attenuate the incident ionizing spectrum seen by components further from the central source. As a result, their ionization equilibrium will be different. If component e is the furthest away from the source and is the only optically thick one, we still need fine tuning to have similar column density ratios in optically thin and optically thick slabs. The higher $\tau_{LL}(e)$ is, the more difficult it is to explain the similar ionization equilibrium in the other components. Based on these arguments we prefer models that fits the data with the smallest $\tau_{LL}(e)$. This is best achieved by choosing incident continuum that yields low temperature. As evident from equation (3), with all else equal, we get higher concentration of He I in the 2^3S level at lower temperatures. A smaller N_{H} is then needed for a given $N_{\text{He I}^*}$, which leads to smaller τ_{LL} . Additional support for lower temperature models come from the Fe II inferred $T < 10,000$ K (see § 2.6).

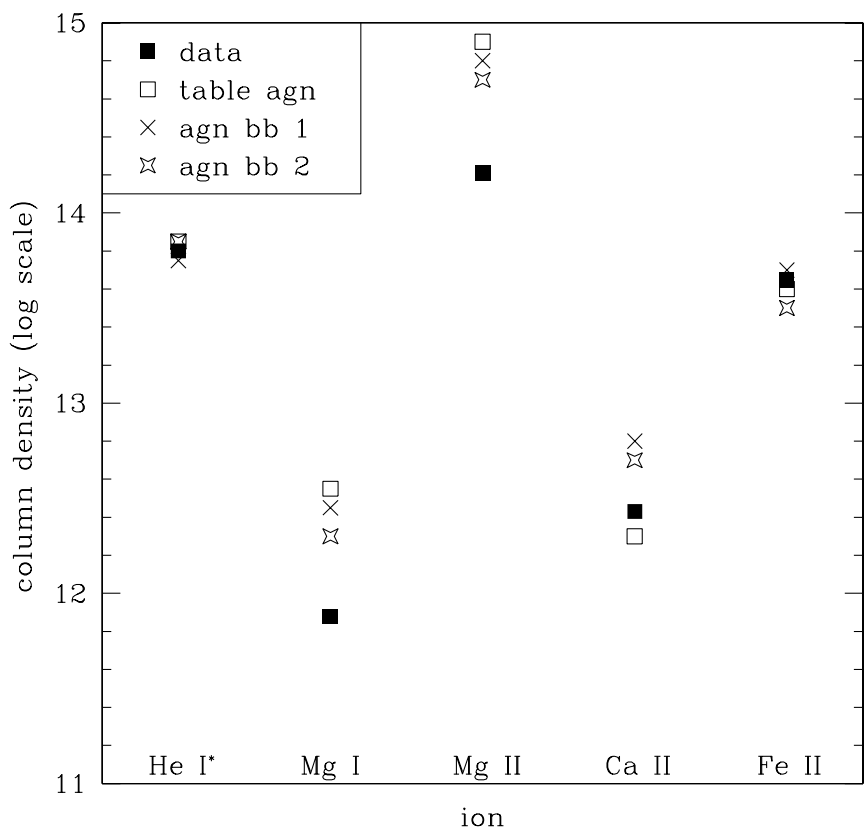


Fig. 9.— Comparison between the observed column densities and simulated ones from three different models. See Table 3 for models' details.

TABLE 3: PHOTOIONIZATION MODELS

| model | $\log(N_{\text{ion}})$ (cm^{-2}) | $\log(U)$ | n_H (cm^{-3}) | τ_{LL} | \bar{T} (10^3 K) |
|-----------|--|-----------|-------------------------------|-------------|-----------------------------------|
| table agn | 20.2 | -2.7 | 10^6 | 6.5 | 12 |
| agn bb 1 | 20.0 | -2.8 | 10^5 | 3.6 | 10 |
| agn bb 2 | 19.9 | -2.7 | 10^5 | 1.5 | 8 |

4.4. Conditions Needed for Detecting Mg I Absorption

In spite of their high S/N, our low-resolution observations do not reveal absorption from Mg I $\lambda 2853$. The reason for this is the small equivalent width of the Mg I features, which in our case can only be detected with a combination of high S/N - high spectral resolution data. As we discuss in § 2 the detection of Mg I puts important constraints on photoionization models. It is therefore important to observe Mg II BALQSOs at high spectral resolution in order to determine the existance of Mg I in the intrinsic absorber.

The ionization models account for the weakness of the Mg I features compared to those of Mg II. For material optically thin at the Lyman edge, figure 7 shows that for a typical AGN spectrum $N_{\text{Mg II}}/N_{\text{Mg I}} \gtrsim 100$ for $-6 < \log(U) < -3$; this result also holds up to $\log(U) = -8$. Thus, for $-8 < \log(U) < -3$ the dominant magnesium ion in absorption is Mg II with Mg I showing roughly 1% of it's column density. That translates to a factor of 30 difference between the optical depths of Mg II $\lambda 2796$ and Mg I $\lambda 2853$. If the Mg II absorber is highly saturated we may detect Mg I absorption even in low-resolution data, as is the case in QSO 1044+3656 (de Kool et al. 2000). Otherwise, only high resolution data can reveal its existance in the deepest parts of the Mg II troughs, which is the case in QSO 2359–1241. In order to detect Mg II at $\log(U) \gtrsim -2$ a hydrogen ionization front is needed (Voit, Weymann & Korista 1993) to keep the relative fraction of Mg II ions high enough. But in that case, we should not expect to see Mg I absorption features. For example, a model using table AGN continuum, $\log(U) = -2$, $N_H = 10^{22} \text{ cm}^{-2}$ (a combination which produces a thick hydrogen ionization front) and $n_H = 10^8 \text{ cm}^{-3}$, predicts that behind the front 99% of the magnesium is in the form of Mg II while only 2×10^{-4} is in Mg I. A good observational example is QSO 0059–2735, where Mg II is detected, Mg I is not (Wampler, Chugai & Petitjean 1995) and a black Lyman limit is observed (Turnshek et al. 1996).

4.5. Relationship Between the High and Low Ionization Absorbers

What is the relationship between the low-ionization absorption (Mg II , Fe II , Mg I...) and the high-ionization absorption (C IV , Si IV , N V...) that are seen in the spectrum of low-ionization BALQSOs? Voit, Weymann & Korista (1993) noted that the low-ionization absorption tends to concentrate at low ejection velocity compared to the high ionization absorption, where the latter normally encompass the velocity range of the former and extends to a much higher velocity. The best examples for that behavior are QSO 0059–2735 and QSO 1232+1325. However, this is not always the case. QSO 0932+5010 shows strong Mg II absorption in its high velocity trough (data courtesy of Ray Weymann and Kirk Korista) and in QSO 2359–1241 we observe a high velocity Mg II trough at -5000 km s^{-1} . As discussed in § 3, our HST UV prism-spectroscopy data show a wide BAL trough in both Si IV and C IV ($\text{FWHM} \sim 8000 \text{ km s}^{-1}$), which encompasses both the high and low velocity troughs seen in Mg II . This relationship strongly suggests that the low-ionization absorption seen in QSO 2359–1241 is indeed physically connected to the BAL flow seen in the UV lines. It appears that a simple picture where the low ionization outflow is confined to low velocity does not hold. A more elaborate model, perhaps including ionization stratification (Arav et al. 1999a), is called for. This picture is strengthen by the observation that in QSO 0059–2735 there is a clear detection of $\text{O VI} \lambda 1034$ BAL (Turnshek et al. 1996). It is very difficult to construct a single-zone ionization model where significant optical depth arises from both Mg II and O VI . We point out that ionization models with large local density gradient give natural explanation for such occurrence (Arav 1996; Arav et al. 1999a) since they allow for material with large variation in ionization parameter to exist at close proximity.

5. SUMMARY

The spectrum of QSO 2359–1241 contains powerful diagnostics for the state of it's outflow. In particular we emphasize the importance of the He I lines from the 2^3S meta-stable level. Under optimal conditions, the abundance of this level is roughly 30 times lower than the abundances of iron and magnesium. Detecting a somewhat higher column density of the He I 2^3S meta-stable level than that of Fe II indicates that 95–99% of the the iron is in higher ionization stages and allows for tight constraints on the ionization parameter. The three well separated He I lines also allow for an excellent saturation/covering-factor analysis, since their oscillator strength differ by a factor of six. With the combined constraints available from the Fe II and He I lines we are able to tightly constrain the ionization equilibrium in the flow; reproduce the observed column densities without invoking departure from solar abundances; and exclude a hydrogen ionization front in this outflow.

A strong connection between the low ionization absorber and the BAL phenomenon is evident in the HST FOC data. High ionization BALs (from C IV, S IV and N V) are detected in the HST data and these encompass and expand the velocity range seen in the low ionization species. It will be very valuable to obtain better HST spectroscopy of the high ionization lines, as well as ground observations of the Al III λ 1857 absorption. These will allow to study the connection between the high and low ionization absorbers in greater detail, and will yield additional constraints on the low-ionization absorber through the Al III λ 1857 and Al II λ 1670 lines.

ACKNOWLEDGMENTS

We thank Kirk Korista, Martijn de Kool and the referee for numerous valuable suggestions. We acknowledge support from NASA HST grant GO-06350, NSF grant AST-9802791 and STScI. Part of this work was performed under the auspices of the US Department of Energy by Lawrence Livermore National Laboratory under Contract W-7405-Eng-48.

REFERENCES

Anderson, K. S. 1974 ApJ, 189, 195

Arav, N., 1996, ApJ, 465, 617

Arav, N., 1997 in Mass Ejection from AGN, ASP Conference Series, Vol. 128, ed. N. Arav, I. Shlosman, and R. J. Weymann, p. 208

Arav, N., Korista, T. K., de Kool, M., Junkkarinen, V. T. & Begelman, M. C. 1999, ApJ, 516, 27. (1999a)

Arav, N., Becker, R. H., Laurent-Muehleisen, S. A., Gregg, M. D., White, R. L., Brotherton, M. S., & de Kool, M. 1999, ApJ, 524, 566 (1999b)

Barlow, T. A., 1997 in Mass Ejection from AGN, ASP Conference Series, Vol. 128, ed. N. Arav, I. Shlosman, and R. J. Weymann, p. 13

reference Barlow, T. A., 2000 in preparation.

Becker, R. H., Gregg, M. D., Hook, I., White, R. L., Helfand, D. J., & McMahon, R. J. 1997, ApJ, 479, L93

Boksenberg, A., Carswell, R. F., Allen, D. A., Fosbury, R. A. E., Penston, M. V., & Sargent, W. L. W. 1977, MNRAS, 178, 451

Boroson, T. A. & Meyers, K. A. 1992, ApJ, 39, 442

Brotherton, M. S., Tran, H. D., van Breugel, W., Dey, A., Antonucci, R. 1997, ApJ, 487, L113

Brotherton, M. S., Wills, B. J.; Dey, A.; van Breugel, W.; Antonucci, R., 1998, ApJ, 501, 110B

Brotherton, M. S., Arav, N., Becker, R. H., Tran, H. D., Gregg, M. D., Laurent-Muehleisen, S. A., White, R. L., & Hack, W. 2000, ApJ, submitted

Churchill, C. W., Schneider, D. P., Schmidt, M., Gunn, J. E., 1999, AJ, 117, 2573

Clegg, R. E. S. 1987, MNRAS, 229, 31

de Kool, M., Arav, N., Becker, R. H., Laurent-Muehleisen, S. A., White, R. L., Price, T., Gregg, M. D. 2000, ApJ, submitted

Ferland, G. J., 1996, University of Kentucky Department of Physics and Astronomy Internal Report

Halpern, J. P., Eracleous, M., Filippenko, A. V. & Chen, K. 1996, ApJ, 464, 704

Hamann, F., Barlow, T. A., Junkkarinen, V. T., & Burbidge, E. M. 1997, ApJ, 478, 80.

MacAlpine, G. M. 1976, ApJ, 204, 694

Mathews, W. G., & Ferland, G. J. 1987, ApJ, 323, 456

Osterbrock, D. E. 1974, *Astrophysics of Gaseous Nebulae* (San Francisco: Freeman)

Oudmaijer, R. D., Busfield, G., & Drew, J. E. 1997, MNRAS, 291, 797

Rudy, R. J., Stocke, J. T. & Foltz, C. B. 1985, ApJ, 288, 531

Telfer, R.C., Kriss, G.A., Zheng, W., Davidson, A.F., & Green, R.F. 1998, ApJ, in press

Turnshek, D. A., et al. 1996, ApJ, 463, 110

Verner, D.A., Verner, E.M., & Ferland, G.J. 1996, Atomic Data & Nuclear Data Tables, 64, 1

Voit, G. M., Weymann, R. J., & Korista, Kirk T. 1993 ApJ, 413, 95

Vogt, S. S., et al. 1994, *Instrumentation in Astronomy VIII*, Proc. SPIE Vol. 2198, Eds. David L. Crawford, Eric R. Craine", 362

Wampler, E. J., Chugai, N. N., & Petitjean, P., 1995, ApJ 443, 586

Weymann, R. J., Morris, S. L., Foltz, C. B., & Hewett, P. C. 1991, ApJ, 373, 23